Wind Turbines Equipped with Fractional-Order Controllers: Stress on the Mechanical Drive Train due to a Converter Control Malfunction

R. Melício, University of Beira Interior, Covilha, Portugal
V. M. F. Mendes, Instituto Superior de Engenharia de Lisboa, Lisbon, Portugal
J. P. S. Catalão*, University of Beira Interior, Covilha, Portugal

Key words:
wind turbines; permanent magnet synchronous generators; modeling; power converters; fractional-order control

This paper is on variable-speed wind turbines with permanent magnet synchronous generator (PMSG). Three different drive train mass models and three different topologies for the power-electronic converters are considered. The three different topologies considered are respectively a matrix, a two-level and a multilevel converter. A novel control strategy, based on fractional-order controllers, is proposed for the wind turbines. Simulation results are presented to illustrate the behavior of the wind turbines during a converter control malfunction, considering the fractional-order controllers. Finally, conclusions are duly drawn.

Received 13 May 2009; Revised 29 December 2009

Nomenclature

u_0	Average wind speed.
u	Wind speed value with disturbance.
A_k	Magnitude of the eigenswing k.
ω_k	Eigenfrequency of the eigenswing k.
P_{tt}	Mechanical power of the turbine.
ρ	Air density.
R	Radius of the area covered by the blades.
c_p	Power coefficient.

* Correspondence to: J. P. S. Catalão, University of Beira Interior, Department of Electromechanical Engineering, R. Fonte do Lameiro, 6201-001 Covilha, Portugal.
E-mail: catalao@ubi.pt

ω_t Rotor angular speed at the wind turbine.

θ Pitch angle of the rotor blades.

λ Tip speed ratio.

P_t Mechanical power of the wind turbine disturbed by the mechanical eigenswings.

m Order of the harmonic of a eigenswing.

g_{km} Distribution of the m-order harmonic in the eigenswing *k*.

a_{km} Normalized magnitude of g_{km}.

h_k Modulation of eigenswing *k*.

φ_{km} Phase of the m-order harmonic in the eigenswing *k*.

J Moment of inertia for blades, hub and generator of the one-mass model.

J_t Moment of inertia for blades and hub of the two-mass model.

T_t Mechanical torque.

T_{dt} Resistant torque in the wind turbine bearing of the two-mass model.

T_{at} Resistant torque in the hub and blades of the two-mass model.

T_{ts} Torsional stiffness torque of the two-mass model.

ω_g Rotor angular speed at the generator.

J_g Moment of inertia for the rotor of the generator.

T_{dg} Resistant torque in the generator bearing of the two-mass model.

T_{ag} Resistant torque due to the viscosity of the airflow in the generator of the two-mass model.

T_g Electric torque.

J_b Moment of inertia of the flexible blades section of the three-mass model.

J_h Moment of inertia of the hub and the rigid blades section of the three-mass model.

T_{db} Resistant torque of the flexible blades of the three-mass model.

T_{bs} Torsional flexible blades stifness torque of the three-mass model.

T_{dh} Resistant torque of the rigid blades and the hub of the three-mass model.

T_{ss} Torsional shaft stifness torque of the three-mass model.

T_{dg} Resistant torque of the generator of the three-mass model.

i_f Equivalent rotor current.

M Mutual inductance.

p Number of pairs of poles.

i_d , i_q Stator currents.

L_d , L_q Stator inductances.

R_d , R_q Stator resistances.

u_d , u_q Stator voltages.

Introduction

In Portugal, the wind power goal foreseen for 2010 was established earlier by the government as 3750 MW, representing about 25% of the total installed capacity by 2010 [1]. But, this wind power goal has now been raised to 5100 MW. Hence, Portugal has one of the most ambitious goals in terms of wind power, and in 2006 was the second country in Europe with the highest wind power growth.

As the penetration level of wind power increases into the power systems, the overall performance of the electric grid will increasingly be affected by the characteristics of wind turbines. One of the major concerns related to the high penetration level of the wind turbines is the impact on power system stability [2]. Also, network operators have to ensure that consumer power quality is not deteriorated. Hence, the total harmonic distortion (THD) should be kept as low as possible, improving the quality of the energy injected into the electric grid [3].

Power-electronic converters have been developed for integrating wind power with the electric grid. The use of power-electronic converters allows not only for variable-speed operation of a wind turbine, but also for enhancement on power extraction [4]. In a recent overview of different wind generator systems [5], it is shown that variable-speed conceptions equipped with power-electronic converters will continue to dominate and be very promising technologies for large wind farms.

Today, variable-speed wind turbines have become more common than traditional fixed-speed turbines [6]. In a variable-speed wind turbine with full-power converter, the wind turbine is directly connected to the generator and the generator is completely decoupled from the electric grid. Of all the generators used in wind turbines, the permanent magnet synchronous generator (PMSG) is the one with a significant advantage: it is stable and secure under normal operating conditions; and comparing with a wound synchronous generator, it is smaller and does not need a direct current power source for field excitation.

Accurate modeling and control of wind turbines have high priority in the research activities all over the world. At the moment, substantial documentation exists on modeling and control issues for the doubly fed induction generator (DFIG) wind turbine. But this is not the case for wind turbines with PMSG and full-power converter [7].

Previous papers were mainly focused on the transient analysis of variable-speed wind turbines at external grid faults [8, 9]. Grid code specifications in European countries require that wind turbines must be able to ride though grid disturbances that bring voltages down to very low levels [10]. Accordingly, great effort has been made to develop variable-speed wind turbines capable of supporting voltage/frequency and remain connected to the system during external grid faults [11, 12], but little attention has been given to the possibility of internal abnormal operating conditions, such as a converter control malfunction, using different drive train mass models. Voltage sags and swells, harmonics, frequency variation, phase steps, DC components and noise, are phenomena that can cause severe malfunction in the control or supervision circuits [13, 14] of the wind turbines. Also, oversimplification on the modeling of the mechanical drive train could introduce significant error in the value of the results [15].

Hence, this paper focuses on the analysis of the stress on the mechanical drive train of wind turbines with PMSG and full-power converters, considering: (i) three different drive train mass models, respectively, one, two and three mass models; (ii) three different topologies for power-electronic converters, respectively matrix, two-level and multilevel converters; (iii) a novel fractional-order control strategy; (iv) a converter control malfunction; (v) the bending flexibility of the blades. Simulation results for the converter control malfunction ascertain the performance of wind turbines equipped with fractional-order controllers.

Modeling

Wind Turbine

The mechanical power of the turbine is given by:

$$P_{tt} = \frac{1}{2}\rho \pi R^2 u^3 c_p \tag{1}$$

The computation of the power coefficient requires the use of blade element theory and the knowledge of blade geometry. In this paper, the numerical approximation developed in [16] is followed, where the power coefficient is given by:

$$c_p = 0.73\left(\frac{151}{\lambda_i} - 0.58\theta - 0.002\theta^{2.14} - 13.2\right)e^{-\frac{18.4}{\lambda_i}} \tag{2}$$

$$\lambda_i = \frac{1}{\frac{1}{(\lambda - 0.02\theta)} - \frac{0.003}{(\theta^3 + 1)}} \tag{3}$$

The global maximum for the power coefficient is at null pitch angle and it is equal to:

$$c_{p\max}(\lambda_{opt}(0), 0) = 0.4412 \tag{4}$$

corresponding to an optimal tip speed ratio at null pitch angle equal to:

$$\lambda_{opt}(0) = 7.057 \tag{5}$$

In order to achieve maximum power, the tip speed ratio at each pitch angle should be kept at the value corresponding to the global maximum for the power coefficient [4]. Hence, the rotor angular speed at the wind turbine is as a function of the maximum mechanical power $P_{tt\max}$, given by:

$$\omega_t = \lambda_{opt}(\theta) \sqrt[3]{\frac{2\ P_{tt\max}}{\rho\ \pi R^5 c_{p\max}(\lambda_{opt}(\theta), \theta)}} \tag{6}$$

A maximum power point tracking (MPPT) is used in determining the optimal rotor angular speed at the wind turbine for each wind speed to obtain maximum rotor power [4].

When regulating the wind system under the specification of maximum power, it must be taken into account that turbine power must never be higher than generator value for the rated power. Once generator rated power is reached at rated wind speed it must be limited. For variable-speed wind turbines, a mechanical actuator is usually employed to change the pitch angle of the blades in order to reduce power coefficient and maintain the power at its rated value. When rated turbine speed is reached, control strategy must be changed so that a higher wind velocity no longer increases turbine speed but increases generated power until generator rated power; increases in rotor speed of about 10% are allowed during transients because of the slow pitch control response [17].

The conversion of wind energy into mechanical energy over the rotor of a wind turbine is influenced by various forces acting on the blades and on the tower of the wind turbine (e.g. centrifugal, gravity and varying aerodynamic forces acting on blades, gyroscopic forces acting on the tower), introducing mechanical effects influencing the energy conversion. Those mechanical effects have been modeled by eigenswings mainly due to the following phenomena: asymmetry in the turbine, vortex tower interaction, and eigenswing in the blades. The mechanical power over the rotor of the wind turbine has been modeled, using the mechanical eigenswings [18], as a set of harmonic terms multiplied by the power associated with the energy capture from the wind by the blades, given by:

$$P_t = P_{tt}\left[1+\sum_{k=1}^{3} A_k\left(\sum_{m=1}^{2} a_{km}\, g_{km}(t)\right) h_k(t)\right] \tag{7}$$

$$g_{km} = \sin\left(\int_0^t m\ \omega_k(t')\ dt' + \varphi_{km}\right) \tag{8}$$

The frequency range of the wind turbine model with mechanical eigenswings is from 0.1 to 10 Hz. The values used on (7) and (8) for the calculation of P_t are given in Table I [18].

"See Table I at the end of the manuscript".

One-Mass Drive Train Model

In a one-mass drive train model, all components are lumped together and modeled as a single rotating mass [15]. The equation for the one-mass model is based on the second law of Newton, deriving the state equation for the rotor angular speed at the wind turbine, given by:

$$\frac{d\omega_t}{dt} = \frac{1}{J}\left(T_t - T_g\right) \tag{9}$$

Two-Mass Drive Train Model

A comparative study of wind turbine generator system using different drive train models [19] has shown that the two-mass model may be more suitable for transient analysis.

The equations for the two-mass model are based on the torsional version of the second law of Newton, deriving the state equation for the rotor angular speed at the wind turbine and for the rotor angular speed at the generator, respectively given by:

$$\frac{d\omega_t}{dt} = \frac{1}{J_t}\left(T_t - T_{dt} - T_{at} - T_{ts}\right) \tag{10}$$

$$\frac{d\omega_g}{dt} = \frac{1}{J_g}\left(T_{ts} - T_{dg} - T_{ag} - T_g\right) \tag{11}$$

Three-Mass Drive Train Model

With the increase in size of the wind turbines, one question arises whether long flexible blades have an important impact on the transient analysis of wind energy systems during a fault [20]. To determine the dynamic properties of the blade, finite element techniques may be used but this approach cannot easily be implemented in power systems analysis programs. Hence, to avoid the use

of the finite element approach it is necessary to simplify the rotor dynamics as much as possible. One way to achieve this is represented in Figure 1, where the blade analysis is represented as a simple torsional system. Since the blade bending occurs at a significant distance from the joint between the blade and the hub, the blade can be split in two parts, OA and AB. The blade sections OA1, OA2 and OA3 establish the moment of inertia of the hub and the rigid section blade and have the moment of inertia J_h, the rest of the blade sections A1B1, A2B2 and A3B3 are the effective flexible blade section and have the moment of inertia J_b [21].

"See *Figure 1* at the end of the manuscript".

The configuration of the three-mass drive train model is shown in Figure 2.

"See *Figure 2* at the end of the manuscript".

The mass moments of inertia for the model are given as input data, but in their absence an estimation of the mass moments of inertia is possible. This estimation is out of the scope of this paper, but it has been researched, for instance in [22].

The equations for the three-mass model are based on the torsional version of the second law of Newton, deriving the state equation for the rotor angular speed at the wind turbine and for the rotor angular speed at the generator, respectively given by:

$$\frac{d\omega_t}{dt} = \frac{1}{J_b}\left(T_t - T_{db} - T_{bs}\right) \tag{12}$$

$$\frac{d\omega_h}{dt} = \frac{1}{J_h}\left(T_{bs} - T_{dh} - T_{ss}\right) \tag{13}$$

$$\frac{d\omega_g}{dt} = \frac{1}{J_g}\left(T_{ss} - T_{dg} - T_g\right) \tag{14}$$

PMSG

The model for the PMSG is the usual one, where the state equations for modeling the PMSG stator currents, using motor machine convention, are given by:

$$\frac{di_d}{dt} = \frac{1}{L_d}\left[u_d + p\,\omega_g\,L_q\,i_q - R_d\,i_d\right] \tag{15}$$

$$\frac{di_q}{dt} = \frac{1}{L_q}\left[u_q - p\,\omega_g\left(L_d\,i_d + M\,i_f\right) - R_q\,i_q\right] \tag{16}$$

In order to avoid demagnetization of permanent magnet in the PMSG, a null stator current $i_d = 0$ is imposed [23]. The electric power is given by:

$$P_g = [u_d \quad u_q \quad u_f][i_d \quad i_q \quad i_f]^T \tag{17}$$

Matrix Converter

The matrix converter is an AC-AC converter, with nine bidirectional commanded insulated gate bipolar transistors (IGBTs) S_{ij}. It is connected between a first order filter and a second order filter. The first order filter is connected to a PMSG, while the second order filter is connected to an electric network. A switching strategy can be chosen so that the output voltages have nearly sinusoidal waveforms at the desired frequency, magnitude and phase angle, and the input currents are nearly sinusoidal at the desired displacement power factor [24]. A three-phase active symmetrical circuit in series models the electric network. The phase currents injected into the electric grid are modeled by the state equation using, given by:

$$\frac{di_{fk}}{dt} = \frac{1}{L_n}(u_{fk} - R_n\, i_{fk} - u_k) \qquad k = \{4,5,6\} \tag{18}$$

The configuration of the simulated wind energy system with matrix converter is shown in Figure 3.

"See *Figure 3* at the end of the manuscript".

The IGBTs commands S_{ij} are given in function of the on and off states, as follows:

$$S_{ij} = \begin{cases} 1, \ (\text{on}) \\ 0, (\text{off}) \end{cases} \qquad i, j \in \{1, 2, 3\} \tag{19}$$

For the matrix converter modeling it is considered that:

$$\sum_{j=1}^{3} S_{ij} = 1 \qquad i \in \{1, 2, 3\} \tag{20}$$

$$\sum_{i=1}^{3} S_{ij} = 1 \qquad j \in \{1, 2, 3\} \tag{21}$$

The vector of output phase voltages is related to the vector of input phase voltages through the command matrix [25], as follows:

$$\begin{bmatrix} v_A \\ v_B \\ v_C \end{bmatrix} = \begin{bmatrix} S_{11} & S_{12} & S_{13} \\ S_{21} & S_{22} & S_{23} \\ S_{31} & S_{32} & S_{33} \end{bmatrix} \begin{bmatrix} v_a \\ v_b \\ v_c \end{bmatrix} = [S] \begin{bmatrix} v_a \\ v_b \\ v_c \end{bmatrix} \tag{22}$$

The vector of input phase currents is related to the vector of output phase currents through the command matrix [25], as follows:

$$[i_a \quad i_b \quad i_c]^T = [S]^T \, [i_A \quad i_B \quad i_C]^T \tag{23}$$

Two-Level Converter

The two-level converter is an AC/DC/AC converter, with six unidirectional commanded IGBTs used as a rectifier, and with the same number of unidirectional commanded IGBTs used as an inverter. Each IGBT is indicated by its switching state S_{ij}. The index i with $i \in \{1,2\}$ identifies the IGBT. A group of two IGBTs linked to the same phase constitute a leg j of the converter. The index j with $j \in \{1,2,3\}$ identifies a leg for the rectifier and $j \in \{4,5,6\}$ identifies the inverter one. The rectifier is connected between the PMSG and a capacitor bank. The inverter is connected between this capacitor bank and a second order filter, which in turn is connected to an electric grid. A three-phase active symmetrical circuit in series models the electric grid [26, 27]. The phase currents injected into the electric grid are modeled by the state equation (18).

The configuration of the wind energy system with two-level converter is shown in Figure 4.

"See *Figure 4* at the end of the manuscript".

A switching variable γ_j of each leg j is used to identify the state of the IGBT i in the leg j of the converter. The switching variable of each leg j [28] is given by:

$$\gamma_j = \begin{cases} 1, \ (S_{1j} = 1 \ \text{and} \ S_{2j} = 0) \\ 0, \ (S_{1j} = 0 \ \text{and} \ S_{2j} = 1) \end{cases} \qquad j \in \{1, \ldots, 6\} \tag{24}$$

Hence, each switching variable depends on the conducting and blocking states of the IGBTs. The voltage v_{dc} is modeled by the state equation, given by:

$$\frac{dv_{dc}}{dt} = \frac{1}{C} \left(\sum_{j=1}^{3} \gamma_j i_j - \sum_{j=4}^{6} \gamma_j i_j \right) \tag{25}$$

Multilevel Converter

The multilevel converter is an AC/DC/AC converter, with twelve unidirectional commanded IGBTs S_{ij} used as a rectifier, and with the same number of unidirectional commanded IGBTs used as an inverter. A group of four IGBTs linked to the same phase constitute a leg j of the converter. The rectifier is connected between the PMSG and a capacitor bank. The inverter is connected between this capacitor bank and a second order filter, which in turn is connected to an electric grid. Again, a three-phase active symmetrical circuit in series models the electric grid [26, 27]. The phase currents injected into the electric grid are modeled by the state equation (18).

The configuration of the wind energy system with multilevel converter is shown in Figure 5.

"See *Figure 5* at the end of the manuscript".

The switching variable γ_j of each leg j is a function of the states S_{ij} of the converter. The index i with $i \in \{1,2,3,4\}$ identifies the IGBT. The index j with $j \in \{1,2,3\}$ identifies the leg for the rectifier and $j \in \{4,5,6\}$ identifies the inverter one. The three valid conditions [29] for the switching variable of each leg j are given by:

$$\gamma_j = \begin{cases} 1, & (S_{1j} \text{ and } S_{2j}) = 1 \quad \text{and} \quad (S_{3j} \text{ or } S_{4j}) = 0 \\ 0, & (S_{2j} \text{ and } S_{3j}) = 1 \quad \text{and} \quad (S_{1j} \text{ or } S_{4j}) = 0 \\ -1, & (S_{3j} \text{ and } S_{4j}) = 1 \quad \text{and} \quad (S_{1j} \text{ or } S_{2j}) = 0 \end{cases} \qquad j \in \{1,\ldots,6\} \tag{26}$$

A switching variable Φ_{1j} is associated with the two upper IGBTs in each leg j (S_{1j} and S_{2j}), and also a switching variable Φ_{2j} is associated with the two lower IGBTs (S_{3j} and S_{4j}), respectively given by:

$$\Phi_{1j} = \frac{\gamma_j(1+\gamma_j)}{2} \quad ; \quad \Phi_{2j} = \frac{\gamma_j(1-\gamma_j)}{2} \qquad j \in \{1,\ldots,6\} \tag{27}$$

Hence, each switching variable depends only on the conducting and blocking states of the IGBTs. The voltage v_{dc} is the sum of the voltages v_{C1} and v_{C2} in the capacitor banks C_1 and C_2, modeled by the state equation, given by:

$$\frac{dv_{dc}}{dt} = \frac{1}{C_1}\left(\sum_{j=1}^{3}\Phi_{1j}i_j - \sum_{j=4}^{6}\Phi_{1j}i_j\right) + \frac{1}{C_2}\left(\sum_{j=1}^{3}\Phi_{2j}i_j - \sum_{j=4}^{6}\Phi_{2j}i_j\right) \tag{28}$$

Control Strategy

Fractional-Order Controller

A novel control strategy based on fractional-order PI^{μ} controllers is studied for the variable-speed operation of wind turbines with PMSG and full-power converters, and its design is more complex than that of classical PI controllers [30]. Fractional-order calculus used in mathematical models of the systems can improve the design, properties and controlling abilities in dynamical systems [31]. Fractional calculus theory is a generalization of ordinary differentiation and integration to arbitrary (non-integer) order [32].

The fractional-order differentiator can be denoted by a general operator ${}_aD_t^{\mu}$ [33], given by:

$$ {}_aD_t^{\mu} = \begin{cases} \dfrac{d^{\mu}}{dt^{\mu}}, & \Re(\mu) > 0 \\ 1, & \Re(\mu) = 0 \\ \int_a^t (d\tau)^{-\mu}, & \Re(\mu) < 0 \end{cases} \tag{29} $$

where μ is the order of derivative or integrals, $\Re(\mu)$ is the real part of the μ. The mathematical definition of fractional derivatives and integrals has been the subject of several descriptions. The most frequently encountered one is called Riemann–Liouville definition, in which the fractional-order integral is given by:

$$ {}_aD_t^{-\mu} f(t) = \frac{1}{\Gamma(\mu)} \int_a^t (t-\tau)^{\mu-1} f(\tau)\, d\tau \tag{30} $$

while the definition of fractional-order derivatives is:

$$ {}_aD_t^{\mu} f(t) = \frac{1}{\Gamma(n-\mu)} \frac{d^n}{dt^n} \left[\int_a^t \frac{f(\tau)}{(t-\tau)^{\mu-n+1}}\, d\tau \right] \tag{31} $$

where:

$$ \Gamma(x) \equiv \int_0^{\infty} y^{x-1} e^{-y}\, dy \tag{32} $$

is the Euler's Gamma function, a and t are the limits of the operation, and μ is the number identifying the fractional order. In this paper, μ is assumed as a real number that satisfies the restrictions $0 < \mu \le 1$. Also, it is assumed that $a = 0$. The following convention is used: ${}_0D_t^{-\mu} \equiv D_t^{-\mu}$.

The other approach is Grünwald–Letnikov definition of fractional-order integral, given by:

$$ {}_{a}D_{t}^{-\mu}\ f(t) = \lim_{h\to 0} h^{\mu} \sum_{r=0}^{\frac{t-a}{h}} \frac{\Gamma(\mu + r)}{r!\Gamma(\mu)} f(t - r\,h) \tag{33} $$

while the definition of fractional-order derivatives is:

$$ {}_{a}D_{t}^{\mu}\ f(t) = \lim_{h\to 0} h^{-\mu} \sum_{r=0}^{\frac{t-a}{h}} (-1)^{r} \frac{\Gamma(\mu + 1)}{r!\Gamma(\mu - r + 1)} f(t - r\,h) \tag{34} $$

where the binomial coefficients $(r > 0)$ are given by: definition, given by:

$$ \binom{\mu}{0} = 1, \quad \binom{\mu}{r} = \frac{\mu(\mu-1)\ \ldots\ (\mu - r + 1)}{r!} \tag{35} $$

The influence of fractional-order controllers is due to their ability for memory. An important property revealed by (33) is that while integer-order operators imply finite series, the fractional-order counterparts are defined by infinite series [31, 33]. This means that integer operators are local operators in opposition with the fractional operators that have, implicitly, a memory of all past events.

The differential equation of the fractional-order PI^{μ} controller, $0 < \mu < 1$, in time domain, is given by:

$$ u(t) = K_p\ e(t) + K_i\ D_t^{-\mu}\ e(t) \tag{36} $$

where K_p is a proportional constant and K_i is an integration constant. Taking $\mu = 1$ in (36), a classical PI controller is obtained. Hence, using Laplace transforms the transfer function of the fractional-order PI^{μ} controller is given by:

$$ G(s) = K_p + K_i\ s^{-\mu} \tag{37} $$

Converters Control

Power converters are variable structure systems, because of the on/off switching of their IGBTs. As mentioned previously, the controllers used in the converters are respectively proportional integral and fractional-order PI^{μ} controllers. Pulse width modulation (PWM) by space vector modulation (SVM) associated with sliding mode is used for controlling the converters.

The sliding mode control strategy presents attractive features such as robustness to parametric uncertainties of the wind turbine and the generator as well as to electric grid disturbances [34].

Sliding mode controllers are particularly interesting in systems with variable structure, such as switching power converters, guaranteeing the choice of the most appropriate space vectors. Their aim is to let the system slide along a predefined sliding surface by changing the system structure.

The power semiconductors present physical limitations that have to be considered during design phase and during simulation study. Particularly, they cannot switch at infinite frequency. Also, for a finite value of the switching frequency, an error $e_{\alpha\beta}$ will exist between the reference value and the control value. In order to guarantee that the system slides along the sliding surface $S(e_{\alpha\beta},t)$, it has been proven that it is necessary to ensure that the state trajectory near the surfaces verifies the stability conditions [25] given by:

$$S(e_{\alpha\beta},t)\ \frac{dS(e_{\alpha\beta},t)}{dt}<0 \tag{38}$$

in practice a small error $\varepsilon>0$ for $S(e_{\alpha\beta},t)$ is allowed, due to power semiconductors switching only at finite frequency. Consequently, a switching strategy has to be considered, given by:

$$-\varepsilon<S(e_{\alpha\beta},t)<+\varepsilon \tag{39}$$

A practical implementation of the switching strategy considered in (39) could be accomplished by using hysteresis comparators.

The outputs of the hysteresis comparators are the integer variables $\sigma_{\alpha\beta}=(\sigma_\alpha,\sigma_\beta)$ [25]. For the two-level converter, σ_α and σ_β assume values in the set Ω given by:

$$\Omega\in\{-1,0,1\} \tag{40}$$

The appropriate vector selection in order to ensure stability for the two-level converter is shown in Table II.

"See Table II at the end of the manuscript".

For the multilevel converter, σ_α and σ_β assume values in the set Ω given by:

$$\Omega\in\{-2,-1,0,1,2\} \tag{41}$$

In this control strategy, only when $v_{C1} \neq v_{C2}$ a new vector is selected. The appropriate vector selection in order to ensure stability for the multilevel converter is shown in Table III, for $v_{C1} > v_{C2}$, and in Table IV, for $v_{C1} < v_{C2}$.

"See Table III at the end of the manuscript".

"See Table IV at the end of the manuscript".

Although wind turbines achieve an excellent technical availability of about 98% on average, they have to face a high number of malfunctions [35]. A severe malfunction in the control can occur due to voltage sags and swells, harmonics, frequency variation, phase steps, DC components and noise [13].

Simulation Results

The mathematical models for the wind energy system with the matrix, two-level and multilevel converters were implemented in Matlab/Simulink. The wind energy system considered has a rated electric power of 900 kW. The time horizon considered in the simulation is 10 s. For the fractional-order PI^{μ} controllers, $\mu = 0.7$ is assumed in this paper. Table V summarizes the wind energy system data.

"See Table V at the end of the manuscript".

The wind speed usually varies considerably and it has been modeled in this paper as a sum of harmonics with frequency range 0.1–10 Hz [18]. The average wind speed considered in this paper is a ramp wind speed starting at 10 m/s and stabilizing at 20 m/s, after 2 s. The wind speed model upstream of the rotor is modeled in this paper by:

$$u(t) = u_0 \left[1 + \sum_k A_k \sin(\omega_k t) \right] \qquad 0 \leq t \leq 10 \tag{42}$$

A converter control malfunction is assumed to occur between 7.00 and 7.02 s, imposing a momentary malfunction on the vector selection for the matrix converter and for the inverter of the two-level and the multilevel converters, simulated by a random selection of vectors constrained to no short circuits on the converters.

Simulations with the model for the matrix converter were carried out, considering one-mass, two-mass and three-mass drive train models in order to establish a comparative behavior. The transient response in the drive train model for the malfunction, a 20 ms power fluctuation, is about 3 s due to the drive train model inertias, shown in Table V.

The rotor speed at the turbine with the one-mass drive train model is shown in Figure 6. It is almost a straight line although the mechanical torque is varying. This is due to the significant moment of the inertia assumed as concentrated in only one-mass.

"See *Figure 6* at the end of the manuscript".

The mechanical torque over the rotor of the wind turbine disturbed by the mechanical eigenswings and the electric torque of the generator, with the one-mass drive train model, are shown in Figure 7. The electric torque of the generator follows the rotor speed at the turbine except when it is decreased due to the malfunction.

"See *Figure 7* at the end of the manuscript".

The rotor speeds at the turbine and at the generator with the two-mass drive train model are shown in Figure 8. The rotor speed at the turbine is almost a straight line as it is for the one-mass drive train. Also, this is due to the significant moment of the inertia associated with the blades and hub. The rotor speed at the generator varies more significantly after the malfunction due to the lesser moment of inertia associated with the generator.

"See *Figure 8* at the end of the manuscript".

The mechanical torque over the rotor of the wind turbine disturbed by the mechanical eigenswings and the electric torque of the generator, with the two-mass drive train model, are shown in Figure 9. The electric torque of the generator follows the rotor speed at the generator except when it is decreased due to the malfunction.

"See *Figure 9* at the end of the manuscript".

The rotor speeds at the turbine and at the generator with the three-mass drive train model are shown Figure 10. Comparing with Figure 8 it is possible to notice the influence of the three-mass modeling as a clear composed harmonic behavior over the speed of the generator.

"See *Figure 10* at the end of the manuscript".

The mechanical torque over the rotor of the wind turbine disturbed by the mechanical eigenswings and the electric torque of the generator, with the three-mass drive train model, are shown in Figure 11. Again, as in Figure 7, the electric torque of the generator follows the rotor speed at the turbine except when it is decreased due to the malfunction.

"See *Figure 11* at the end of the manuscript".

In order to compare the behavior for the drive train models, the rotor speeds at the turbine with the three different mass drive train models are shown in Figure 12. While the rotor speeds at the turbine with the one-mass and with the two-mass models are in a tight neighborhood, the rotor speed at the turbine with three-mass model is lesser all the time, justifying the increase on the mechanical torque in comparison with the other two models.

"See *Figure 12* at the end of the manuscript".

This comparison is in favor of the three-mass model, since it offers a more realistic dynamic behavior for the drive train.

The currents injected into the electric grid for the wind energy system with matrix converter and with the three-mass drive train model are shown in Figure 13. As expected during the malfunction they decrease, but almost after the end of the malfunction they recover to their normal behavior.

"See *Figure 13* at the end of the manuscript".

The voltage v_{dc} for the two-level converter with a three-mass drive train model is shown in Figure 14. As expected during the malfunction this voltage increases, the capacitor is charged, but almost after the end of the malfunction it recovers to its normal value.

"See *Figure 14* at the end of the manuscript".

The currents injected into the electric grid for the wind energy system with two-level converter and with the three-mass drive train model are shown in Figure 15. As expected during the malfunction they decrease, but almost after the end of the malfunction they recover to their normal behavior.

"See *Figure 15* at the end of the manuscript".

The voltage v_{dc} for the multilevel converter with a three-mass drive train model is shown in Figure 16. The behavior of this voltage is identical to the one with the two-level converter.

"See *Figure 16* at the end of the manuscript".

The currents injected into the electric grid for the wind energy system with multilevel converter and with the three-mass drive train model are shown in Figure 17. As expected during the malfunction they decrease, but almost after the end of the malfunction they recover to their normal behavior.

"See *Figure 17* at the end of the manuscript".

For the same fault conditions, the transient response of the three-mass drive train model is larger than that of the one-mass or the two-mass model.

Conclusions

This paper reports a study for PMSG variable-speed wind turbines, considering three different drive train mass models and three different topologies for the power-electronic converters. Our study deals with the transient analysis during an internal fault, namely a converter control malfunction. The contributions of this paper are threefold: ascertaining the transient behavior at an internal fault using matrix, two-level and multilevel converters; using a novel control strategy based on fractional-order controllers; and investigating the effects of the bending flexibility of blades. The simulation results have shown that the consideration of the bending flexibility of blades can influence the wind turbine response during internal faults. Hence, the three-mass drive train model, including both blades and shaft flexibilities, may be more appropriate for the transient analysis of wind energy systems.

References

1. Estanqueiro A, Castro R, Flores P, Ricardo J, Pinto M, Rodrigues R, Peças Lopes J. How to prepare a power system for 15% wind energy penetration: the Portuguese case study. *Wind Energy* 2008; **11**: 75-84.
2. Ullah NR, Thiringer T. Effect of operational modes of a wind farm on the transient stability of nearby generators and on power oscillations: a Nordic grid study. *Wind Energy* 2008; **11**: 63-73.
3. Carrasco JM, Franquelo LG, Bialasiewicz JT, Galvan E, Guisado RCP, Prats AM, Leon JI, Moreno-Alfonso N. Power-electronic systems for the grid integration of renewable energy sources: A survey. *IEEE Trans. Ind. Electron.* 2006; **53**: 1002-1016.
4. Baroudi JA, Dinavahi V, Knight AM. A review of power converter topologies for wind generators. *Renew. Energy* 2007; **32**: 2369-2385.
5. Li H, Chen Z. Overview of different wind generator systems and their comparisons. *IET Renew. Power Gener.* 2008; **2**: 123-138.
6. Ackermann T. (ed.). *Wind Power in Power Systems*. John Wiley and Sons Ltd.: West Sussex, 2005.
7. Hansen AD, Michalke G. Modelling and control of variable-speed multi-pole permanent magnet synchronous generator wind turbine. *Wind Energy* 2008; **11**: 537-554.
8. Jauch C. Transient and dynamic control of a variable speed wind turbine with synchronous generator. *Wind Energy* 2007; **10**: 247-269.
9. Kasem AH, El-Saadany EF, El-Tamaly HH, Wahab MAA. An improved fault ride-through strategy for doubly fed induction generator-based wind turbines. *IET Renew. Power Gener.* 2008; **2**: 201-214.

10. Conroy JF, Watson R. Aggregate modelling of wind farms containing full-converter wind turbine generators with permanent magnet synchronous machines: transient stability studies. *IET Renew. Power Gener.* 2009; **3**: 39-52.
11. Ramtharan G, Ekanayake JB, Jenkins N. Frequency support from doubly fed induction generator wind turbines. *IET Renew. Power Gener.* 2007; **1**: 3-9.
12. Kanellos FD, Hatziargyriou ND. Control of variable speed wind turbines equipped with synchronous or doubly fed induction generators supplying islanded power systems. *IET Renew. Power Gener.* 2009; **3**, 96-108.
13. Martins AP. A DFT-based phasor estimation method for power electronics converter control and protection under strong grid voltage perturbations. *Euro. Trans. Electr. Power* 2009; **19**: 1082-1097.
14. Jaskulski IW, Pinheiro H, Mariotto L. Multi-leg voltage source converter for grid connected wind turbines. *Proceedings of ICCEP'07*, 2007; 229-235.
15. Salman SK, Teo ALJ. Windmill modeling consideration and factors influencing the stability of a grid-connected wind power-based embedded generator. *IEEE Trans. Power Systems* 2003; **18**: 793-802.
16. Slootweg JG, de Haan SWH, Polinder H, Kling WL. General model for representing variable speed wind turbines in power system dynamics simulations. *IEEE Trans. Power Syst.* 2003; **28**: 144-151.
17. Chinchilla M, Arnaltes S, Burgos JC. Control of permanent-magnet generators applied to variable-speed wind energy systems connected to the grid. *IEEE Trans. Energy Convers.* 2006; **21**: 130-135.
18. Akhmatov V, Knudsen H, Nielsen AH. Advanced simulation of windmills in the electric power supply. *Int. J. Electr. Power Energy Syst.* 2000; **22**: 421-434.
19. Muyeen SM, Hasan Ali M, Takahashi R, Murata T, Tamura J, Tomaki Y, Sakahara A, Sasano E. Transient stability analysis of grid connected wind turbine generator system considering multi-mass shaft modeling. *Electr. Power Compon. Syst.* 2006; **34**: 1121-1138.
20. Li H, Chen Z. Transient stability analysis of wind turbines with induction generators considering blades and shaft flexibility. *Proceedings of 33rd IEEE IECON*, 2007; 1604-1609.
21. Ramtharan G, Jenkins N. Influence of rotor structural dynamics representations on the electrical transient performance of DFIG wind turbines. *Wind Energy* 2007; **10**: 293-301.
22. Muyeen SM, Ali MH, Takahashi R, Murata T, Tamura J, Tomaki Y, Sakahara A, Sasano E. Comparative study on transient stability analysis of wind turbine generator system using drive train models. *IET Renewable Power Generation.* 2007; **1**: 131-141.

23. Senjyu T, Tamaki S, Urasaki N, Uezato K. Wind velocity and position sensorless operation for PMSG wind generator. *Proceedings of 5th PEDC*, 2003; 787-792.
24. Barakati SM, Aplevich JD, Kazerani M. Controller design for a wind turbine system including a matrix converter. *Proceedings 2007 IEEE PES GM*, 2007.
25. Pinto S, Silva J. Sliding mode direct control of matrix converters. *IET Electr. Power Appl.* 2007; **1**: 439-448.
26. Melício R, Mendes VMF, Catalão JPS. Two-level and multilevel converters for wind energy systems: a comparative study. *Proceedings of the 13th EPE-PEMC*, 2008; 1682-1687.
27. Melício R, Mendes VMF, Catalão JPS. Evaluating power quality in wind power generation systems with two-level and multi-level converters. *Proceedings of the 6th MedPower Conf.*, 2008.
28. Silva JF, Pinto SF. *Control Methods for Switching Power Converters*. Academic Press, 2007; 935-998.
29. Barros JD, Silva JF. Optimal predictive control of three-phase NPC multilevel converter for power quality applications. *IEEE Trans. Ind. Electron.* 2008; **55**; 3670-3681.
30. Arijit B, Swagatam D, Ajith A, Sambarta D. Design of fractional-order PI-lambda-D-mu-controllers with an improved differential evolution. *Eng. Appl. Artif. Intell.* 2009; **22**: 343-350.
31. Jun-Yi C, Bing-Gang C. Design of fractional order controllers based on particle swarm optimization. *Proceedings of IEEE ICIEA 2006*, 2006; 1-6.
32. Podlubny I. Fractional-order systems and PI-lambda-D-mu-controllers. *IEEE Trans. Autom. Control* 1999; **44**: 208-214.
33. Calderón AJ, Vinagre BM, Feliu V. Fractional order control strategies for power electronic buck converters. *Signal Processing* 2006; **86**: 2803-2819.
34. Beltran B, Ahmed-Ali T, Benbouzid MEH. Sliding mode power control of variable-speed wind energy conversion systems. *IEEE Trans. Energy Convers.* 2008; **23**: 551-558.
35. Hahn B, Durstewitz M, Rohrig K. Reliability of wind turbines. Renewable Energies Knowledge 2006. www.renknow.net.

Figure captions

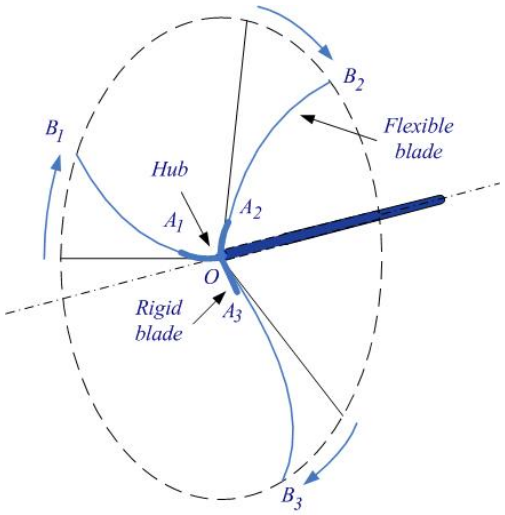

Figure 1. Blade bending dynamics for the three-mass drive train model

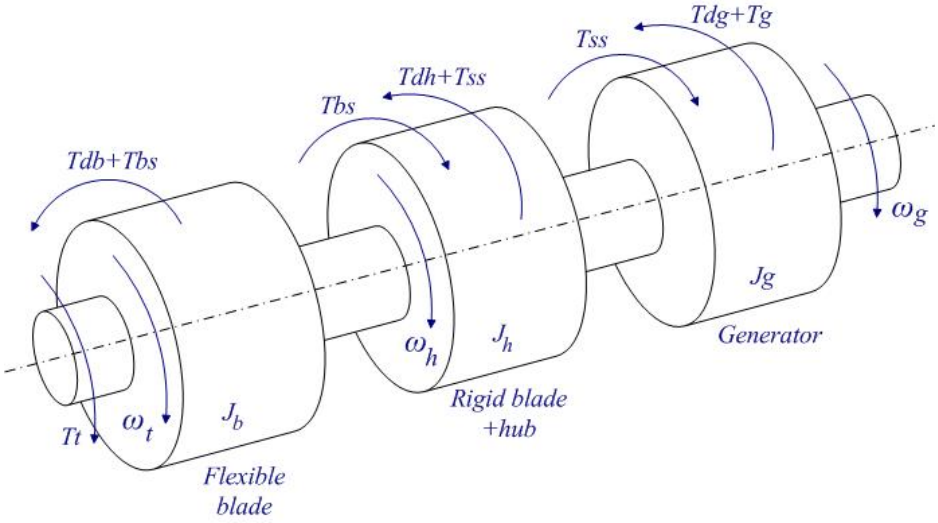

Figure 2. Configuration of the three-mass drive train model

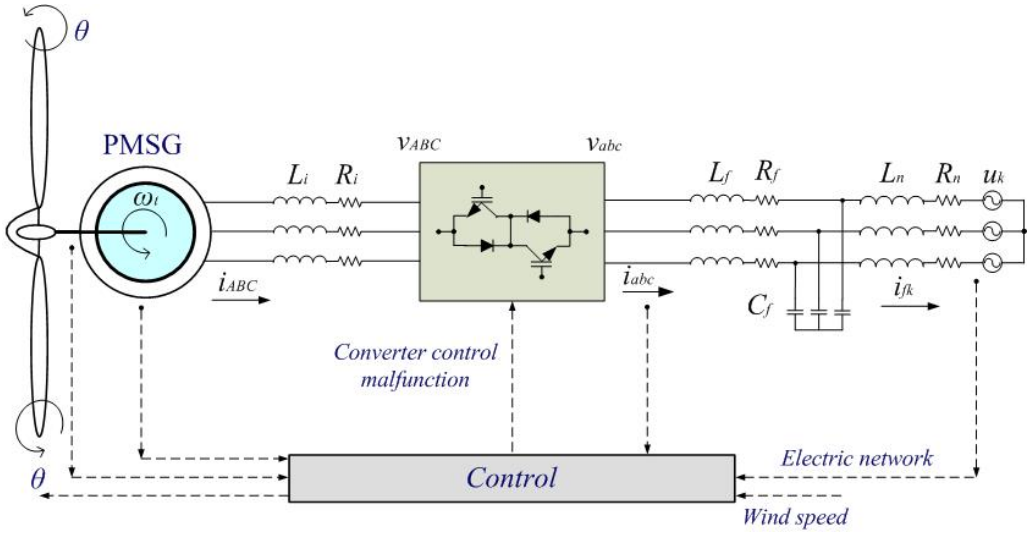

Figure 3. Wind energy system with matrix converter

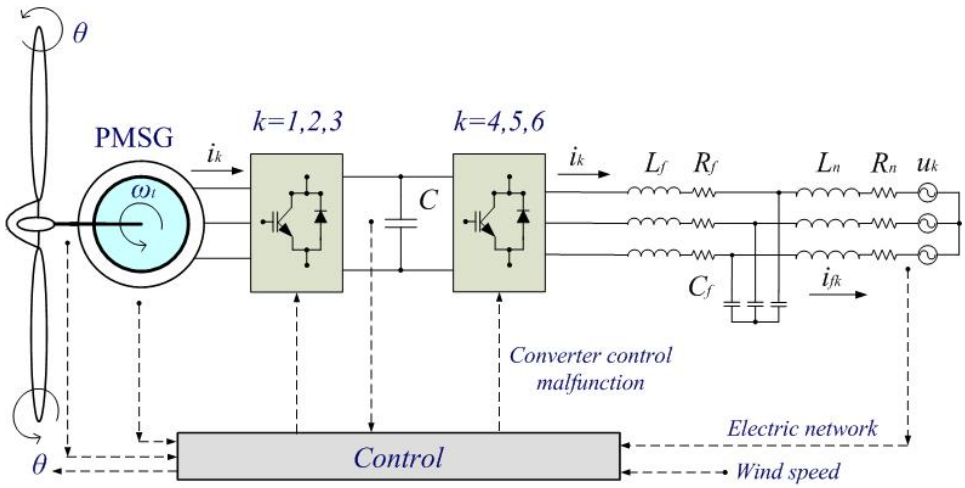

Figure 4. Wind energy system with two-level converter

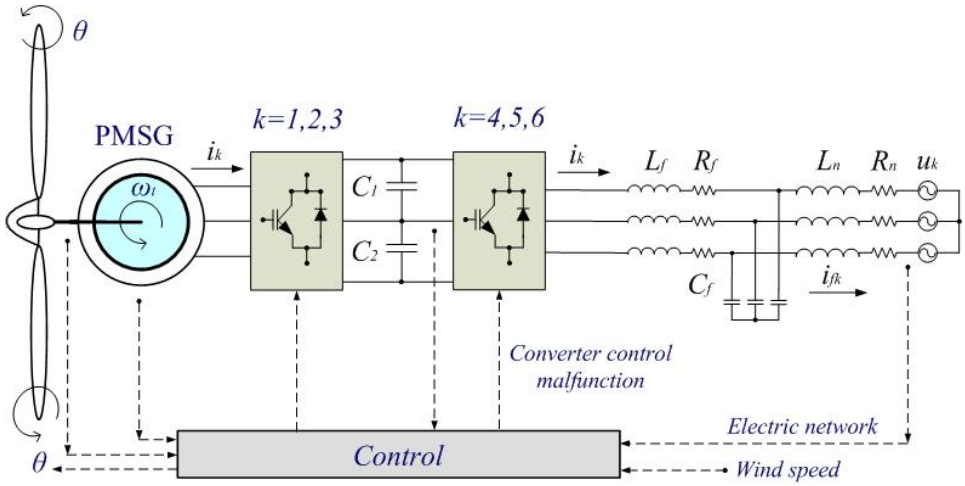

Figure 5. Wind energy system with multilevel converter

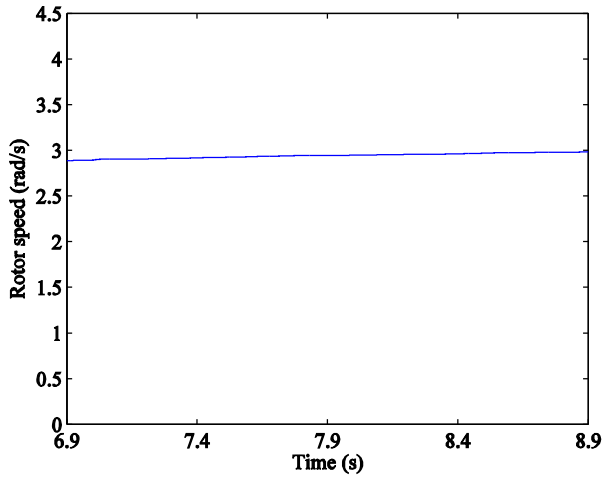

Figure 6. Rotor speed at the turbine with the one-mass drive train model, considering matrix converter

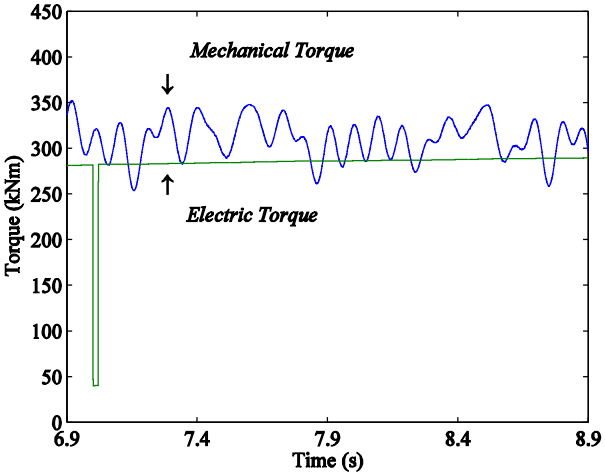

Figure 7. Mechanical and electric torque with the one-mass drive train model, considering matrix converter

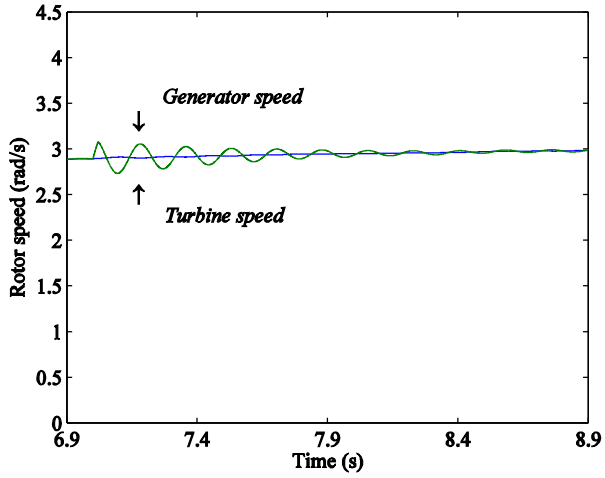

Figure 8. Rotor speeds at the turbine and at the generator with the two-mass drive train model, considering matrix converter

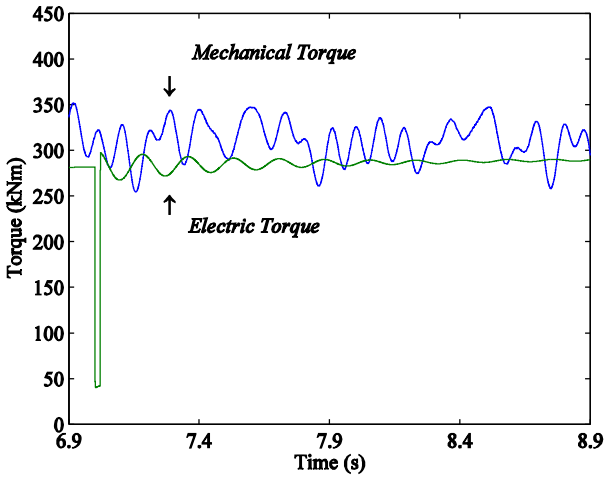

Figure 9. Mechanical and electric torque with the two-mass drive train model, considering matrix converter

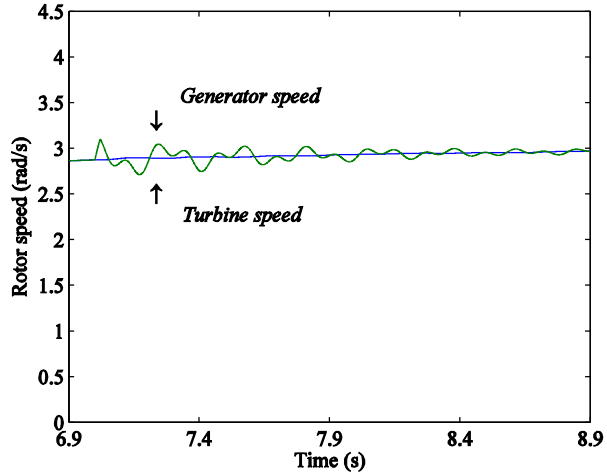

Figure 10. Rotor speeds at the turbine and at the generator with the three-mass drive train model, considering matrix converter

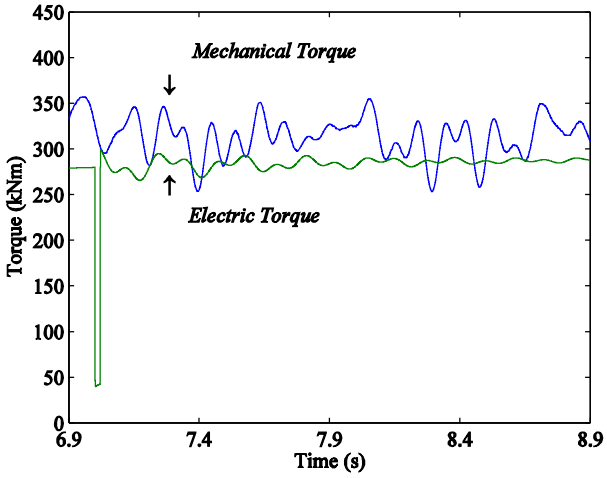

Figure 11. Mechanical and electric torque with the three-mass drive train model, considering matrix converter

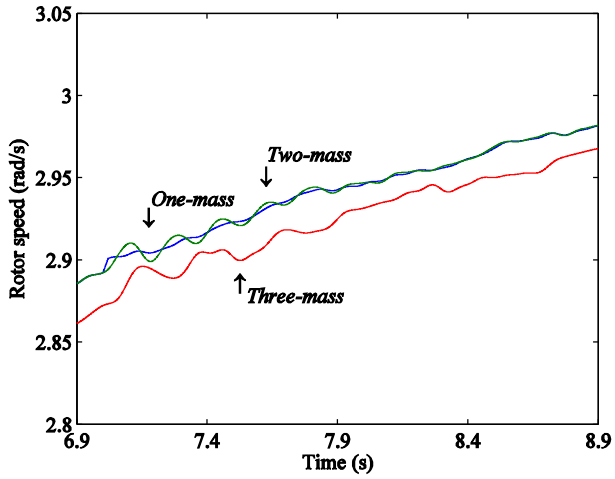

Figure 12. Rotor speeds at the turbine with the three different mass drive train models, considering matrix converter

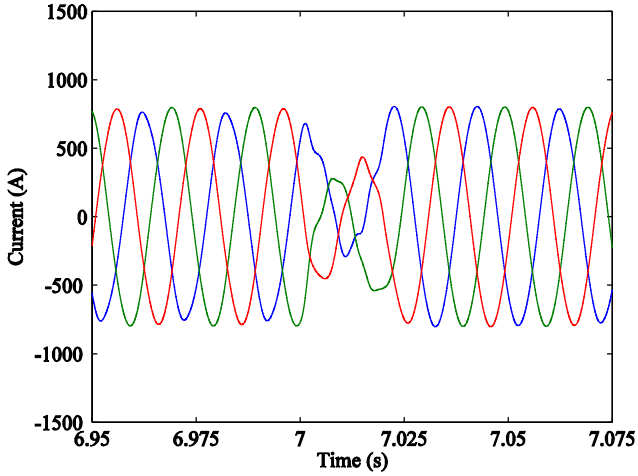

Figure 13. Currents injected into the electric grid (matrix converter and three-mass drive train model)

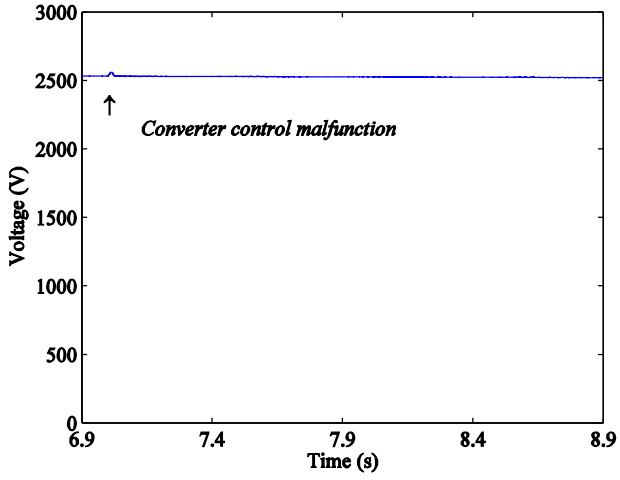

Figure 14. Voltage v_{dc} for the two-level converter with a three-mass drive train model

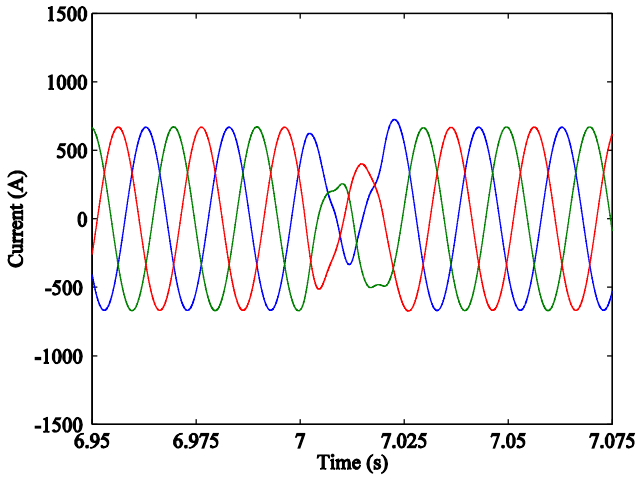

Figure 15. Currents injected into the electric grid (two-level converter and three-mass drive train model)

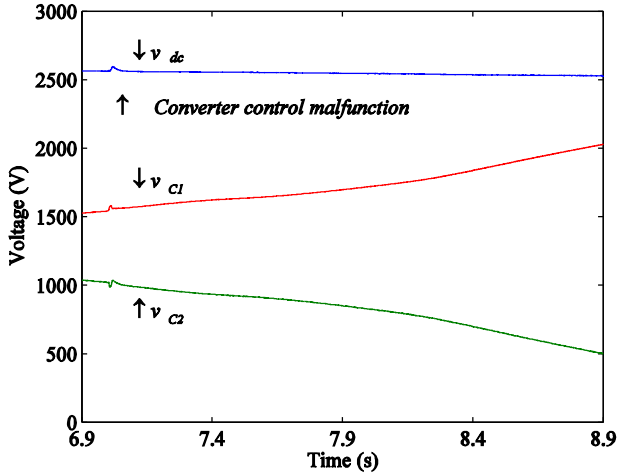

Figure 16. Voltage v_{dc} for the multilevel converter with a three-mass drive train model

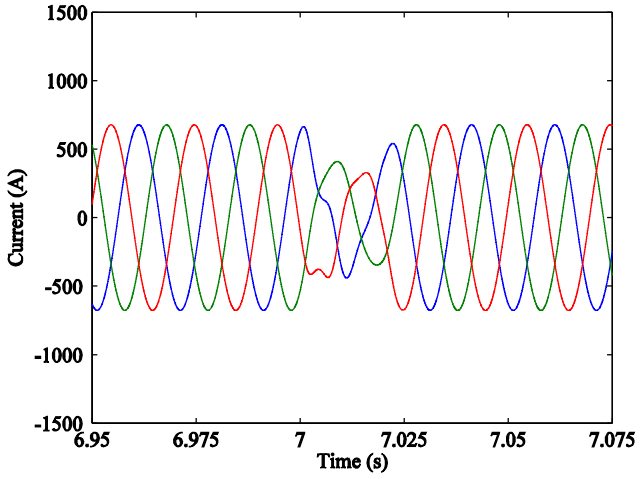

Figure 17. Currents injected into the electric grid (multilevel converter and three-mass drive train model)

Tables

Table I. Mechanical eigenswings excited in the wind turbine

k	Source	A_k	ω_k [rad/s]	h_k	m	a_{km}	φ_{km}
1	Asymmetry	0.01	ω_t	1	1	4/5	0
					2	1/5	$\pi/2$
2	Vortex tower interaction	0.08	$3\,\omega_t$	1	1	1/2	0
					2	1/2	$\pi/2$
3	Blades	0.15	$9\,\pi$	$1/2\,(g_{11}+g_{21})$	1	1	0

Table II. Output voltage vectors selection for the two-level converter

$\sigma_\beta \setminus \sigma_\alpha$	-1	0	1
-1	4	4;5	5
0	6	0;7	1
1	2	3;2	3

Table III. Output voltage vectors selection for the multilevel converter, for $v_{C1} > v_{C2}$

$\sigma_\beta \setminus \sigma_\alpha$	-2	-1	0	1	2
-2	25	25	12	7	7
-1	24	13	13;6	6	8
0	19	18	1;14;27	5	9
1	20	17	17;2	2	4
2	21	21	16	3	3

Table IV. Output voltage vectors selection for the multilevel converter, for $v_{C1} < v_{C2}$

$\sigma_\beta \setminus \sigma_\alpha$	-2	-1	0	1	2
-2	25	25	12	7	7
-1	24	26	26;11	11	8
0	19	23	1;14;27	10	9
1	20	22	22;15	15	4
2	21	21	16	3	3

Table V. Wind energy system data

Blades moment of inertia	400×10^3 kgm²
Hub moment of inertia	19.2×10^3 kgm²
Generator moment of inertia	16×10^3 kgm²
Stiffness	1.8×10^6 Nm
Turbine rotor diameter	49 m
Tip speed	17.64-81.04 m/s
Rotor speed	6.9-30.6 rpm
Generator rated power	900 kW